Nano Research

Open Access

Research Article

Activating lithium storage in 2D $CaSi_2$ anode via enhancing pseudocapacitive properties with oxygen modification engineering

Yongzheng Zhang[2], Lu Sun[3] ✉, Kailin Yang[1], Youwang Ye[1], Liang Zhan[2], Qi Wei[4] ✉, and Jianan Gu[1] ✉

[1] *Institute of Energy Power Innovation, North China Electric Power University, Beijing 100096, China*
[2] *State Key Laboratory of Chemical Engineering, East China University of Science and Technology, Shanghai 200237, China*
[3] *State Key Laboratory of Mesoscience and Engineering, Institute of Process Engineering, Chinese Academy of Sciences, Beijing 100190, China*
[4] *Aviation Key Laboratory of Science and Technology on Advanced Surface Engineering, AVIC Manufacturing Technology Institute, Beijing 100024, China*

Cite this article: *Nano Research*, **2025**, *18*, 94907277. https://doi.org/10.26599/NR.2025.94907277

ABSTRACT: Silicon (Si) has emerged as a promising anode material for lithium-ion batteries (LIBs) due to its extremely high theoretical capacity of 4200 mAh·g^{-1}. However, its practical application is limited by several critical challenges, including severe volume expansion and poor electrical conductivity. Herein, we employ a two-dimensional (2D) oxygen modification engineering approach to fabricate 2D oxygen-functionalized $CaSi_2$ ($CaSi_2O_x$) layers. During the preparation of 2D $CaSi_2$ layers, O atoms are gradually incorporated onto their surface. The resulting 2D $CaSi_2O_x$ layers have a thickness of 3–5 nm, closely matching the theoretical thickness of 6–10 layers. When used as lithium anodes, the 2D $CaSi_2O_x$ layers exhibit exceptional electrochemical performance, maintaining stability over 3000 cycles at an ultrahigh current density of 30 A·g^{-1}. By tailoring the surface properties, their pseudocapacitive charge storage mechanism is significantly enhanced, effectively overcoming the intrinsic limitations of traditional Si anodes. This study highlights the promise of 2D surface engineering in the development of advanced materials for next-generation LIBs.

KEYWORDS: two-dimensional (2D) $CaSi_2O_x$, Si anode, volume change, pseudocapacitive, surface modification, lithium storage

1 Introduction

Lithium-ion batteries (LIBs) have become an integral part of daily life, powering various devices and technologies [1–4]. However, their development has been constrained by the limitations of commercial graphite anodes, which have a relatively low theoretical capacity of 372 mAh·g^{-1} [5]. In contrast, silicon (Si) has emerged as a promising anode material for LIBs due to its extremely high theoretical capacity of 4200 mAh·g^{-1}, significantly surpassing that of commercial graphite anodes [6–8]. However, its practical application is limited by several critical challenges, including severe volume expansion (> 300%) during lithiation and delithiation, low Coulombic efficiency (CE), and poor electrical conductivity [9, 10]. These issues result in electrode pulverization, the formation of an unstable solid electrolyte interphase (SEI) layer, loss of electrical contact, and rapid capacity degradation.

Thus, researchers have turned their attention to Si composite anodes or Si-alloy anodes [11–15]. To improve the electrochemical performance of Si-based anodes, three main strategies have been proposed to address the above challenges: dimension nanostructuring, alloying with other metals, and controlled surface oxidation [16, 17]. The strategy of dimension nanostructuring involves the preparation of silicon-based structures in various dimensional forms, such as zero-dimensional (0D) (Si nanospheres) [18, 19], one-dimensional (1D) (Si nanowires) [20–22], and two-dimensional (2D) (few-layer silicene) [23, 24]. Among these, 2D engineering is regarded as the most promising approach due to the unique structures, which can effectively mitigate volume expansion, shorten the diffusion paths of Li^+ ion, and enhance ion transport. For instance, when few-layer silicene was used for lithium storage, it demonstrated remarkable cycling stability, achieving up to 1800 cycles with a reversible capacity of 800 mAh·g^{-1} [25]. This performance is significantly superior to other 0D and 1D structures tested under the similar conditions. In addition to nanostructuring, Si alloying with other metals is an

Received: December 8, 2024; **Revised:** January 17, 2025
Accepted: January 27, 2025

✉Address correspondence to Lu Sun, lsun@ipe.ac.cn; Qi Wei, weiq057@avic.com; Jianan Gu, gujianan@ncepu.edu.cn

efficient strategy to improve electrical conductivity and reduce internal resistance. For example, the introduction of metallic germanium (Ge) to form a SiGe alloy significantly improved the electrochemical performance, achieving a capacity of 1046 mAh·g^{-1} at 2 A·g^{-1} after 500 cycles [26]. The alloying process helps stabilize the electrode structure and improves its durability during repeated lithiation and delithiation cycles. Recently, controlling the surface oxides of Si-based anodes has emerged as a promising approach to enhance their practical applicability by improving the pseudocapacitive properties for lithium storage [27]. This strategy not only enhances cycling stability but also reduces the production cost of the anodes. Prof. Guo and his co-workers developed a $SiMg_yO_x$ anode that delivered a 1000-cycle operational life under industry-standard electrochemical testing conditions [28]. The improved pseudocapacitive behavior of these materials is crucial for stabilizing the electrode/electrolyte interface and maintaining high performance during extended cycling.

These strategies have been proven effective in addressing the challenges of Si anodes, even when only one or two are applied. However, simultaneously integrating all three strategies within a single electrode material remains a challenge, because it is difficult to fabricate Si alloy materials with a 2D structure. Among these Si-based alloy materials, $CaSi_2$ stands out as a unique candidate due to its intrinsic 2D structure [29, 30]. This inherent advantage makes $CaSi_2$ an excellent platform for combining 2D nanostructuring, alloying, and surface oxidation within a single material. By leveraging these combined strategies, the electrochemical limitations of Si-based anodes can be addressed more comprehensively, enabling their practical implementation in next-generation LIBs.

Herein, we employ a 2D oxygen modification engineering approach to fabricate 2D oxygen-functionalized $CaSi_2$ ($CaSi_2O_x$) layers. During the preparation of 2D $CaSi_2$ layers, O atoms are gradually incorporated onto their surface. The resulting 2D $CaSi_2O_x$ layers have a thickness of 3–5 nm, closely matching the theoretical thickness of 6–10 layers. When used as anode in LIBs, the 2D $CaSi_2O_x$ layers exhibit exceptional electrochemical performance, maintaining stability over 3000 cycles at an ultrahigh current density of 30 A·g^{-1}. By tailoring the surface properties, the pseudocapacitive charge storage was highly enhanced, effectively overcoming the intrinsic limitations of traditional Si anodes. This study highlights the promise of 2D surface engineering in the development of advanced materials for next-generation LIBs.

2 Experimental

2.1 The synthesis of 2D $CaSi_2O_x$ layers and 2D $CaSi_2$ layers

To prepare 2D $CaSi_2O_x$ and $CaSi_2$ layers, $CaSi_2$ powders were initially dispersed in isopropyl alcohol (IPA) at a concentration of 1 mg·mL^{-1} to form separate suspensions. For the synthesis of $CaSi_2O_x$ layers, the dispersion was sonicated in an air atmosphere without any gas protection to induce partial surface oxidation, while the preparation of 2D $CaSi_2$ layers was carried out under an inert pure argon (Ar) atmosphere to preserve the pristine structure. Specifically, 200 mg of $CaSi_2$ powder was introduced into 200 mL of IPA, pre-saturated with either air or Ar gas, followed by ultrasonication for 24 h. This sonication process facilitated the exfoliation of $CaSi_2$ into few-layered nanosheets, with the degree of exfoliation increasing with prolonged sonication. After sonication, the resulting products were thoroughly washed with deionized water and ethanol several times to remove residual impurities.

2.2 Morphological and structural characterization

The samples were characterized extensively to analyze their morphology and microstructure. Atomic force microscopy (AFM) was employed to capture detailed surface topography and texture. Transmission electron microscopy (TEM) and selected area electron diffraction (SAED) were carried out on a Tecnai G2 F20 U-TWIN system to reveal the nanoscale structural arrangement. X-ray diffraction (XRD) was performed using a Rigaku D/max2500PC with Cu Kα radiation over a 2θ range of 10°–80° to confirm the crystalline structure and phase composition. Raman spectroscopy, conducted with a Horiba JY LaRAM ARAMIS system, was utilized to probe the vibrational properties of the materials. X-ray photoelectron spectra were recorded by a Thermo Electron Corporation ESCALAB 250 XPS spectrometer using a monochromatized Al Kα radiation with 200 eV pass energy with 30 eV step over the sample (500 μm × 500 μm).

2.3 Electrochemical measurements

Electrochemical performance was evaluated using 2032 coin-type cells. The working electrodes were prepared by mixing the active material, acetylene black, and polyvinylidene fluoride (PVDF) in a weight ratio of 7:2:1. The resulting slurry was evenly coated onto Cu foil, with an active material mass loading of ~ 0.5 mg·cm^{-2}. Pure lithium foil served as the counter electrode, while a polypropylene film was used as the separator. The electrolyte consisted of 1.0 M $LiPF_6$ dissolved in a 1:1 weight ratio mixture of ethylene carbonate and dimethyl carbonate. Charge–discharge tests were conducted on a Land CT2001A battery testing system across a range of current densities (0.16 to 30 A·g^{-1}) within a voltage window of 0.01–3.00 V. Electrochemical impedance spectroscopy (EIS) measurements were performed using a CHI760E electrochemical workstation.

3 Results and discussion

Figure 1 illustrates the preparation process of 2D $CaSi_2O_x$ and 2D $CaSi_2$ layers via a sonication-assisted exfoliation approach under controlled atmospheres (air and Ar). $CaSi_2$ is a typical layered material composed of alternating Si and Ca layers (Fig. S1 in the Electronic Supplementary Material (ESM)), making it an excellent precursor for the production of 2D nanosheets. In this preparation process, IPA was employed as the exfoliation medium, and the sonication facilitates the delamination of $CaSi_2$ into individual or few-layered nanosheets. The exfoliation was performed under two distinct atmospheric conditions to tailor the surface properties and oxidation states of the materials. In an oxygen/air atmosphere, the process induced partial oxidation of 2D $CaSi_2$ layer, resulting in the formation of 2D $CaSi_2O_x$ layers. Oxygen atoms were introduced into the surface of $CaSi_2$ during sonication and caused the surface oxidation, likely altering the electronic structure and creating additional active sites for lithium storage. Conversely, exfoliation in an Ar atmosphere inhibited oxidation and preserved the pristine layered structure of $CaSi_2$. The resulting 2D $CaSi_2$ nanosheets retained their intrinsic properties, making them suitable for applications requiring unmodified $CaSi_2$.

SEM measurements were employed to examine the morphology of the 2D $CaSi_2O_x$ layers and $CaSi_2$ bulk. As exhibited in Figs. S2

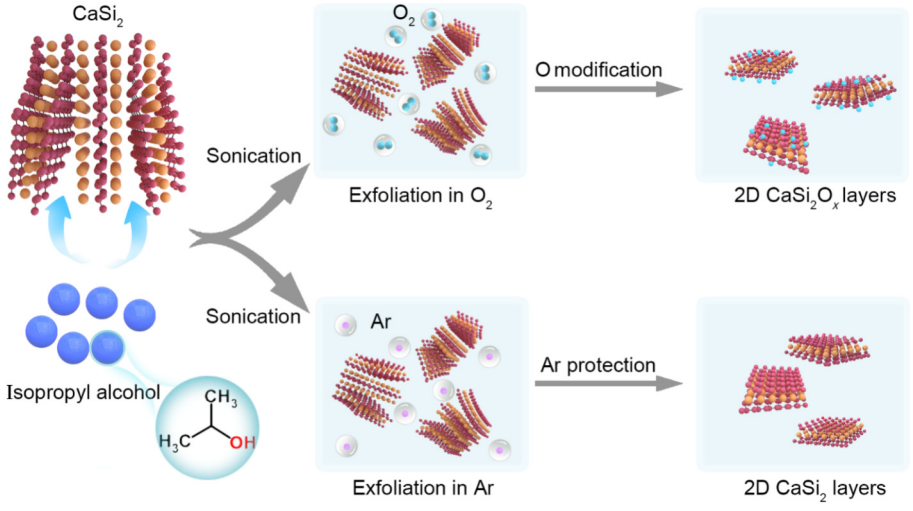

Figure 1 Schematic illustration of the preparation of 2D $CaSi_2O_x$ and 2D $CaSi_2$ layers.

and S3 in the ESM, the $CaSi_2O_x$ layers demonstrate a 2D layered morphology compared to $CaSi_2$ bulk. Furthermore, the TEM images (Fig. 2(a) and Fig. S4 in the ESM) reveal their ultrathin, sheet-like morphology, which are different from the original $CaSi_2$ bulk (Fig. S5 in the ESM). These observations confirm the successful exfoliation of the layered $CaSi_2$ structure into 2D nanosheets, highlighting the effectiveness of the oxidation-assisted sonication process. Besides, the high-resolution TEM (Fig. 2(b)) image further demonstrates the crystalline nature of the 2D $CaSi_2O_x$ layers, as evidenced by distinct lattice fringes. The measured lattice spacing of 3.06 Å corresponds to the (104) plane, verifying the retention of the material's crystallographic structure during the oxidation-assisted exfoliation process. Furthermore, the SAED pattern (inset image) exhibits sharp diffraction spots, providing additional confirmation of the crystallinity of the 2D $CaSi_2O_x$ layers. AFM measurement was also conducted to examine the thickness of the 2D $CaSi_2O_x$ layers (Fig. 2(c)). The AFM image shows smooth, flat sheets with a consistent thickness, and the line profile inset indicates a thickness of 3–5 nm, corresponding to 6–10 layers of $CaSi_2$. This measurement corresponds to a few-layer structure, in agreement with the TEM observations, and demonstrates the success of the exfoliation process in producing well-defined 2D nanosheets.

XRD patterns of the 2D $CaSi_2O_x$ layers, 2D $CaSi_2$ layers, and pristine $CaSi_2$ reveal similar diffraction peaks, indicating that the crystalline structure remains unchanged (Fig. 2(d)). However, a closer examination of the (006) diffraction peak highlights structural differences among the three samples. The increased peak intensity of (006) observed in the 2D $CaSi_2O_x$ layers suggests successful exfoliation of the $CaSi_2$ into thinner nanosheets (Fig. 2(e) and Fig. S6 in the ESM). Meanwhile, the intensity in the (0018) and (0024) peaks show a distinct decrease compared to pristine $CaSi_2$

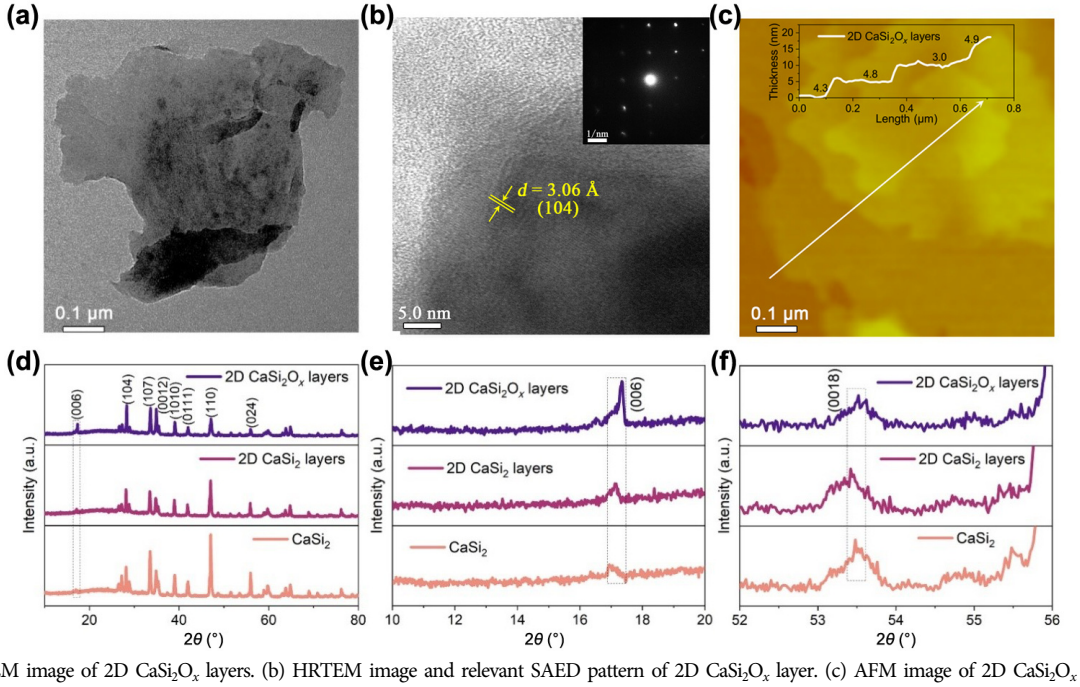

Figure 2 (a) TEM image of 2D $CaSi_2O_x$ layers. (b) HRTEM image and relevant SAED pattern of 2D $CaSi_2O_x$ layer. (c) AFM image of 2D $CaSi_2O_x$ layer. (d) XRD patterns of 2D $CaSi_2O_x$ layers, 2D $CaSi_2$ layers, and $CaSi_2$, respectively. Magnified XRD patterns of (e) (006) and (f) (0018) peaks of 2D $CaSi_2O_x$ layers, 2D $CaSi_2$ layers, and $CaSi_2$, respectively.

(Fig. 2(f) and Figs. S7 and S8 in the ESM), indicating that the exfoliation process has effectively reduced the interlayer thickness, resulting in thinner, more layered structures. A similar phenomenon has been observed in the preparation of other 2D materials, such as MXenes, where the exfoliation process enhances the separation between layers [31–39]. These results confirm that the oxidation-assisted exfoliation process preserves the overall crystal structure while significantly altering the layer thickness and enhancing the 2D nature of the material.

The Raman spectra display distinct peaks for the 2D $CaSi_2O_x$ layers, 2D $CaSi_2$ layers, and pristine $CaSi_2$ (Fig. 3(a)). In the pristine $CaSi_2$, a strong peak near 516 cm^{-1} is observed, which corresponds to the Si–Si stretching vibration within the layered $CaSi_2$ structure (Fig. 3(b) and Fig. S9 in the ESM) [40]. For the 2D $CaSi_2$ layers, this characteristic peak is retained but shows slight broadening and a red shift, indicating minor structural distortions introduced by the exfoliation process. These distortions likely arise from the reduction in layer thickness and subtle changes in the interlayer interactions. Similar phenomena have been observed in the exfoliation of other 2D materials, such as antimonene and MoS_2 [41, 42]. In the case of the 2D $CaSi_2O_x$ layers, the peak shifts further toward lower wavenumbers (red shift) and broadens significantly. This pronounced red shift should be attributed to the formation of Si–O bonds due to the partial oxidation. The incorporation of O atoms alters the local bonding environment, enhancing the Si–Si vibration and decreasing the vibrational frequency. These spectral changes confirm the successful preparation of the 2D $CaSi_2O_x$ layers during the oxidation-assisted exfoliation process.

The XPS spectra of 2D $CaSi_2O_x$ layers, 2D $CaSi_2$ layers, and $CaSi_2$ further confirm the presence of Si 2p, Ca 2p, O 1s, and C 1s signals without any other elements (Fig. 3(c) and Figs. S10 and S11 in the ESM). The prominent O 1s peak and high ratio of Si and O (Table S1 in the ESM) indicate significant surface oxidation, consistent with the Raman results. The Si 2p spectra (Fig. 3(d)) show two main components: a lower binding energy peak at ~ 99.5 eV (Si–Si bond) and a higher binding energy peak at ~ 103 eV (Si–O bond). For pristine $CaSi_2$, the Si–Si peak dominates, indicating the intact silicide structure. In 2D $CaSi_2$ layers, the Si–Si peak remains dominant with minimal Si–O contribution, reflecting the preservation of the silicide framework. In 2D $CaSi_2O_x$ layers, the Si–O peak becomes dominant, evidencing substantial oxidation of Si atoms on the surface, consistent with the formation of 2D $CaSi_2O_x$ layers. The Ca 2p spectra exhibit peaks corresponding to Ca–Si (~ 348.5 eV) and Ca–O (~ 347 eV) environments (Fig. 3(e)). In pristine $CaSi_2$, the Ca–Si peak dominates, indicating Ca's interaction with the silicide lattice. For 2D $CaSi_2$ layers, this peak shifts slightly due to lattice distortions during exfoliation. In 2D $CaSi_2O_x$ layers, the Ca–O and Ca–Si peaks shift to higher energy, indicating the increase valence of Ca due to the oxidation. The O 1s spectra show peaks attributed to O–Si (~ 531.5 eV), O–Ca (~ 530.5 eV), and possibly O–Si–Ca species (Fig. 3(f)). For pristine $CaSi_2$, the O–Si–Ca peak is dominant. In 2D $CaSi_2$ layers, weak O-related peaks emerge, suggesting minor surface oxidation during exfoliation. In 2D $CaSi_2O_x$ layers, the O 1s peak intensifies significantly, dominated by O–Si–O and O–Ca bonds, consistent with surface oxidation and the formation of mixed oxides. These results highlight the successful modulation of surface chemistry through controlled oxidation, which is critical for the electrochemical properties.

To evaluate the electrochemical performance of the 2D $CaSi_2O_x$ layers, a half-cell configuration was fabricated, consisting of a 2D $CaSi_2O_x$ anode, a lithium counter electrode, and a separator (Fig. 4(a)). The cyclic voltammetry (CV) curves for the first and second cycles reveal distinct peaks corresponding to the lithiation and delithiation processes (Fig. 4(b) and Fig. S12 in the ESM). The cathodic peak at ~ 1.46 V appears during the first cycle but disappears in the second cycle, which can be attributed to the formation of a SEI film. The peaks at ~ 0.94 and 1.00 V are likely associated with the insertion and extraction of Li^+ ions into and from the 2D $CaSi_2O_x$ layers. The redox peaks at 0.01 and 0.05 V are most likely related to the lithiation and delithiation processes involving Li and Ca or Si. The charge–discharge voltage profiles of the 2D $CaSi_2O_x$ layers during the 1st, 2nd, and 50th cycles demonstrate a gradual stabilization of the reversible capacity (Fig. 4(c)), reflecting

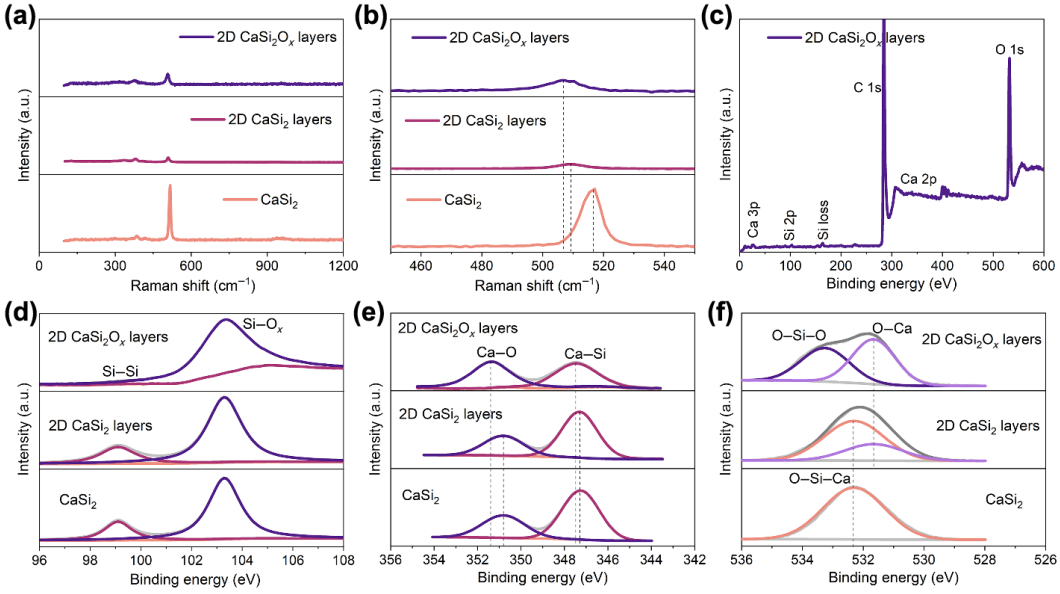

Figure 3 (a) Raman shift and (b) magnified spectra of 2D $CaSi_2O_x$ layers, 2D $CaSi_2$ layers, and $CaSi_2$, respectively. (c) XPS spectrum of 2D $CaSi_2O_x$ layers. (d) High-resolution XPS spectra of Si 2p of 2D $CaSi_2O_x$ layers, 2D $CaSi_2$ layers, and $CaSi_2$, respectively. (e) High-resolution XPS spectra of Ca 2p of 2D $CaSi_2O_x$ layers, 2D $CaSi_2$ layers, and $CaSi_2$, respectively. (f) High-resolution XPS spectra of O 1s of 2D $CaSi_2O_x$ layers, 2D $CaSi_2$ layers, and $CaSi_2$, respectively.

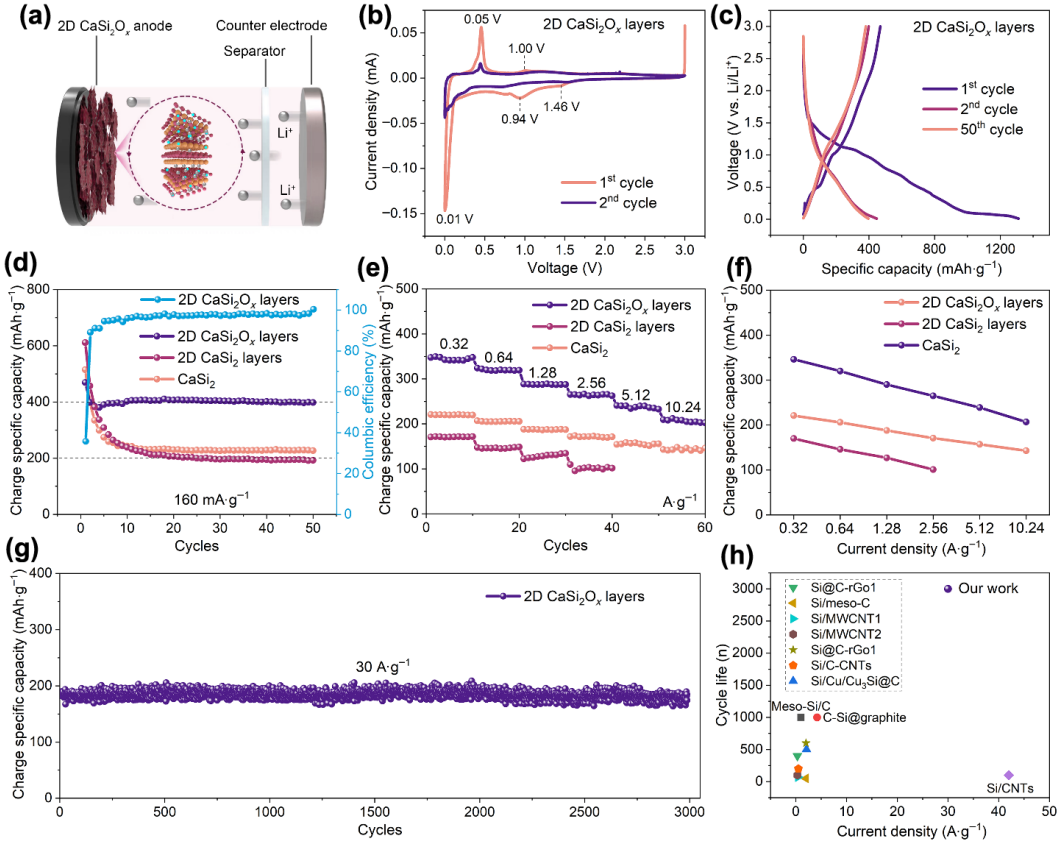

Figure 4 (a) Schematic illustration of battery based on $CaSi_2O_x$ anode and Li counter electrode. (b) CV curves of 2D $CaSi_2O_x$ layers for the first two cycles. (c) Selected charge–discharge curves of 2D $CaSi_2O_x$ of 1st, 2nd, and 50th cycles. (d) Cyclic performance and CE of 2D $CaSi_2O_x$ layers, 2D $CaSi_2$ layers, and $CaSi_2$, respectively. (e) and (f) Rrate capabilities of 2D $CaSi_2O_x$ layers, 2D $CaSi_2$ layers, and $CaSi_2$, respectively, at various current densities. (g) Long cyclic performance of 2D $CaSi_2O_x$ layers at a current density of 30 A·g^{-1}. (h) Comparison of electrochemical performance between 2D $CaSi_2O_x$ layers and reported Si-based anodes.

the formation of a stable SEI film and enhanced cycling stability. When comparing cycling performance (Fig. 4(d)), the 2D $CaSi_2O_x$ layers outperform the 2D $CaSi_2$ layers (Fig. S13 in the ESM) and pristine $CaSi_2$ (Fig. S14 in the ESM) in terms of both specific capacity and retention. At a current density of 160 mA·g^{-1}, the 2D $CaSi_2O_x$ layers maintain a significantly higher specific capacity of ~ 400 mAh·g^{-1} over 50 cycles, underscoring the beneficial effects of surface oxidation. Besides, the 2D $CaSi_2O_x$ layers exhibit a ~ 100% Coulumbic efficiency after 50 cycles. The rate capability tests (Figs. 4(e) and 4(f)) further highlight the superior performance of the 2D $CaSi_2O_x$ layers, which exhibit the highest specific capacities across various current densities compared to the 2D $CaSi_2$ layers and $CaSi_2$. This good rate performance should be attributed to the abundant O functional groups and improved charge-transfer kinetics introduced by surface oxidation. Notably, at an ultrahigh current density of 30 A·g^{-1}, the 2D $CaSi_2O_x$ layers demonstrate exceptional long-term cycling stability, maintaining a consistent specific capacity up to 200 mAh·g^{-1} over 3000 cycles. SEM measurements were further conducted to investigate electrode structure of $CaSi_2O_x$. As shown in Figs. S15 and S16 in the ESM, the SEM images of 2D $CaSi_2O_x$ electrodes before and after cycling show the stability and integrality of electrode, ensuring the long cycle life. This excellent electrochemical performance is superior to those of reported Si-based anodes (Fig. 4(h) and Table S2 in the ESM) [43–52]. This outstanding performance underscores the material's robustness and its potential for high-rate energy storage applications.

To explore the mechanism underlying the high-performance lithium storage of 2D $CaSi_2O_x$ layers, CV measurements (Figs. S17 and S18 in the ESM) at various scan rates and EIS tests were performed. These analyses provide insights into the charge storage behavior, reaction kinetics, and ion transport properties, which are critical for understanding the superior electrochemical performance of the electrode material. Figure 5(a) shows the relationship between the logarithm of the peak current (log(i)) and the logarithm of the sweep rate (log(v)) for the 2D $CaSi_2O_x$ layers and pristine $CaSi_2$. The slope b of this plot is a key parameter that indicates the dominant charge storage mechanism. For pristine $CaSi_2$, the b-value is 0.19, suggesting a diffusion-controlled process, where the lithium-ion insertion/extraction depends primarily on solid-state diffusion. For the 2D $CaSi_2O_x$ layers, the b-value is significantly higher at 0.71, indicating a predominance of pseudocapacitive behavior, where charge storage involves surface-driven, fast redox reactions rather than slow ion diffusion. Figure 5(b) quantifies the contribution of capacitive-controlled (purple) and diffusion-controlled (orange) processes at various scan rates for the 2D $CaSi_2O_x$ layers. At lower scan rates (0.2 mV·s^{-1}), the diffusion-controlled contribution is higher (~ 32.5%), as the slower rate allows sufficient time for lithium-ion diffusion into the electrode material. However, as the scan rate increases, the capacitive-controlled contribution dominates, reaching at 87.7% at 3.0 mV·s^{-1}. This shift reflects the surface-dominated charge storage behavior facilitated by the 2D structure and O functional group, which enhance the availability of active sites and improve charge-

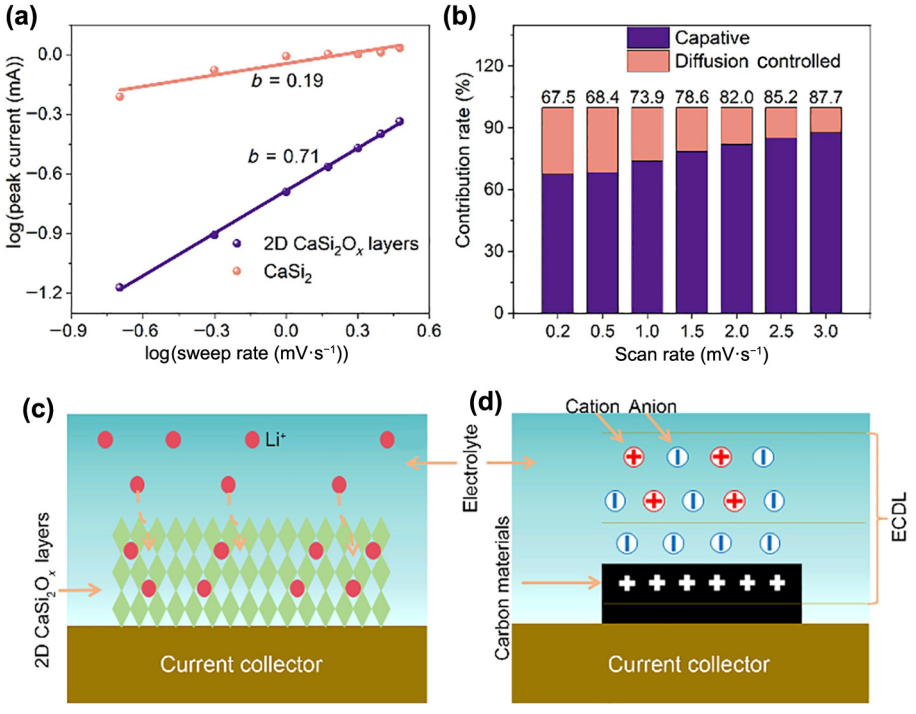

Figure 5 (a) The relationship between the logarithm of the peak current (log(*i*)) and the logarithm of the sweep rate (log(*v*)) for the 2D $CaSi_2O_x$ layers and pristine $CaSi_2$. (b) The contribution of capacitive-controlled (purple) and diffusion-controlled (orange) processes at various scan rates for the 2D $CaSi_2O_x$ layers. (c) The pseudocapacitance mechanism of 2 D $CaSi_2O_x$ layers for lithium storage. (d) Schematic illustration of traditional electrochemical double-layer capacitance.

transfer kinetics. Besides, the fitting EIS curves demonstrate that 2D $CaSi_2O_x$ layers possess lower inter resistance than that of $CaSi_2$ (Figs. S19 and S20 and Table S3 in the ESM), ensuring the fast Li^+ ions transfer.

The exceptional performance of 2D $CaSi_2O_x$ layers can be attributed to their intercalation pseudocapacitance mechanism (Fig. 5(c)), which enables rapid lithium-ion storage and excellent cycling stability. Unlike traditional electrochemical double-layer capacitance (Fig. 5(d)), where charge storage is purely electrostatic, intercalation pseudocapacitance involves fast surface-limited redox reactions. The layered structure of 2D $CaSi_2O_x$ provides accessible intercalation pathways, minimizing ion diffusion distances and enhancing charge-transfer kinetics. Additionally, the partially oxidized surface introduces abundant active sites, further boosting redox activity and pseudocapacitive behavior. These features collectively lead to high specific capacity, superior rate performance, and long-term cycling stability, making 2D $CaSi_2O_x$ layers highly suitable for high-rate energy storage applications.

4 Conclusions

We adopt a 2D oxygen functionalization strategy to synthesize 2D $CaSi_2O_x$ layers by gradually incorporating oxygen atoms onto the surface of 2D $CaSi_2$ during preparation. The fabricated 2D $CaSi_2O_x$ layers exhibit a thickness of 3–5 nm, aligning well with the theoretical thickness of 6–10 layers of $CaSi_2$. As the anode materials in LIBs, the 2D $CaSi_2O_x$ layers demonstrate exceptional electrochemical performance, maintaining stability for over 3000 cycles at an ultrahigh current density of 30 $A{\cdot}g^{-1}$. The surface functionalization enhances the pseudocapacitive charge storage mechanism, addressing the inherent challenges of conventional Si anodes. These advantages result in a high specific capacity, excellent rate performance, and remarkable cycling stability, highlighting the suitability of 2D $CaSi_2O_x$ layers for high-rate energy storage applications.

Electronic Supplementary Material: Supplementary material (SEM and TEM iamges, XRD and Raman spectras, CV curves and EIS results) is available in the online version of this article at https://doi.org/10.26599/NR.2025.94907277.

Data availability

All data needed to support the conclusions in the paper are presented in the manuscript and the Electronic Supplementary Material. Additional data related to this paper may be requested from the corresponding author upon request.

Acknowledgements

This work is supported partially by project of the National Natural Science Foundation of China (Nos. 62474064 and 52102203), the Fundamental Research Funds for the Central Universities (No. 2024MS082), and the NCEPU "Double First-Class" Program.

Declaration of competing interest

All the contributing authors report no conflict of interests in this work.

Author contribution statement

Y. Z. Z.: Data curation, validation, writing manuscript, experimental design. L. S.: Data curation, project administration, experimental design. K. L. Y.: Project administration, data curation, writing manuscript. Y. W. Y.: Data curation, project administration. Q. W.: Project administration, writing manuscript. J. N. G.: Project

administration, funding acquisition, writing manuscript. All the authors have approved the final manuscript.

Use of AI statement

None.

References

[1] Hu, B.; Xu, J.; Fan, Z. J.; Xu, C.; Han, S. C.; Zhang, J. X.; Ma, L. B.; Ding, B.; Zhuang, Z. C.; Kang, Q. et al. Covalent organic framework based lithium-sulfur batteries: Materials, interfaces, and solid-state electrolytes. *Adv. Energy Mater.* **2023**, *13*, 2203540.

[2] Kang, Q.; Zhuang, Z. C.; Liu, Y. J.; Liu, Z. H.; Li, Y.; Sun, B.; Pei, F.; Zhu, H.; Li, H. F.; Li, P. L. et al. Engineering the structural uniformity of gel polymer electrolytes via pattern-guided alignment for durable, safe solid-state lithium metal batteries. *Adv. Mater.* **2023**, *35*, 2303460.

[3] Kang, Q.; Li, Y.; Zhuang, Z. C.; Wang, D. S.; Zhi, C. Y.; Jiang, P. K.; Huang, X. Y. Dielectric polymer based electrolytes for high-performance all-solid-state lithium metal batteries. *J. Energy Chem.* **2022**, *69*, 194–204.

[4] Kang, Q.; Zhuang, Z. C.; Li, Y.; Zuo, Y. Z.; Wang, J.; Liu, Y. J.; Shi, C. Q.; Chen, J.; Li, H. F.; Jiang, P. K. et al. Manipulating dielectric property of polymer coatings toward high-retention-rate lithium metal full batteries under harsh critical conditions. *Nano Res.* **2023**, *16*, 9240–9249.

[5] Kang, Q.; Li, Y.; Zhuang, Z. C.; Yang, H. J.; Luo, L. X.; Xu, J.; Wang, J.; Guan, Q. H.; Zhu, H.; Zuo, Y. Z. et al. Engineering a dynamic solvent-phobic liquid electrolyte interphase for long-life lithium metal batteries. *Adv. Mater.* **2024**, *36*, 2308799.

[6] Tu, J. X.; Yu, S.; Hao, K.; Sun, L.; Bai, R. C.; Zhang, F. Z.; Li, A. J.; Liu, H. Controllable synthesis of one-dimensional silicon nanostructures based on the dual effects of electro-deoxidation and the Kirkendall effect. *Nano Res.* **2024**, *17*, 7814–7823.

[7] Vanpeene, V.; Huet, L.; Villanova, J.; Olbinado, M.; Marone, F.; Maire, E.; Roué, L.; Devic, T.; Lestriez, B. Deciphering the benefits of coordinated binders in Si-based anodes by combined operando/*in situ* and *ex situ* X-ray micro- and nano-tomographies. *Adv. Energy Mater.* **2024**, in press, https://doi.org/10.1002/aenm.202403741.

[8] Gu, J. N.; Zhang, Y. Z.; Shi, Y.; Jin, Y. L.; Chen, H.; Sun, X.; Wang, Y. H.; Zhan, L.; Du, Z. G.; Yang, S. B. et al. Heteroatom immobilization engineering toward high-performance metal anodes. *ACS Nano* **2024**, *18*, 25966–25985.

[9] Yan, Z. L.; Yi, S.; Wang, Z.; Ning, P. P.; Zhang, J. W.; Huang, J. L.; Xiao, Y. M.; Yang, D. R.; Zhang, Y. G.; Du, N. Atomic-level regulation of SiC_4 units enable high Li^+ dynamics and long-life micro-size SiC_x anodes. *Adv. Energy Mater.* **2024**, *14*, 2400598.

[10] Yu, Y. Y.; Yang, C.; Jiang, Y.; Shang, Z. T.; Zhu, J. D.; Zhang, J. H.; Jiang, M. J. Robust nitrogen/sulfur Co-doped carbon frameworks as multifunctional coating layer on Si anodes toward superior lithium storage. *Adv. Energy Mater.* **2025**, *15*, 2403086.

[11] Luo, J.; Arnot, D. J.; King, S. T.; Kingan, A.; Nicoll, A.; Tong, X.; Bock, D. C.; Takeuchi, E. S.; Marschilok, A. C.; Yan, S. et al. Two-dimensional siloxene nanosheets: Impact of morphology and purity on electrochemistry. *ACS Appl. Mater. Interfaces* **2023**, *15*, 24306–24318.

[12] Xie, J.; Sun, L.; Liu, Y. X.; Xi, X. G.; Chen, R. Y.; Jin, Z. SiO_x/C–Ag nanosheets derived from Zintl phase $CaSi_2$ via a facile redox reaction for high performance lithium storage. *Nano Res.* **2022**, *15*, 395–400.

[13] Liu, C. W.; Lau Jr, V.; Tsui, L. Y.; Loo, B. Q.; Hsu, H. P.; Lan, C. W. Exfoliability of two-dimensional silicon nanosheets from calcium disilicide and its enhanced performance as lithium-ion battery anode material. *J. Energy Storage* **2023**, *72*, 108399.

[14] Sun, L.; Xie, J.; Huang, S. C.; Liu, Y. X.; Zhang, L.; Wu, J.; Jin, Z. Rapid CO_2 exfoliation of Zintl phase $CaSi_2$-derived ultrathin free-standing Si/SiO_x/C nanosheets for high-performance lithium storage. *Sci. China Mater.* **2022**, *65*, 51–58.

[15] Sun, L.; Su, T. T.; Xu, L.; Liu, M. P.; Du, H. B. Two-dimensional ultra-thin SiO_x ($0 < x < 2$) nanosheets with long-term cycling stability as lithium ion battery anodes. *Chem. Commun.* **2016**, *52*, 4341–4344.

[16] Li, M. L.; Xue, D. C.; Rong, Z. Y.; Fang, R. Y.; Wang, B.; Liang, Y. L.; Zhang, X. D.; Huang, Q.; Wang, Z. Y.; Zhu, L. Y. et al. Stack pressure enhanced size threshold of Si anode fracture in all-solid-state batteries. *Adv. Funct. Mater.* **2024**, in press, https://doi.org/10.1002/adfm.202415696.

[17] Zhou, P.; Xiao, P.; Pang, L.; Jiang, Z.; Hao, M.; Li, Y.; Wu, F. X. High-performance yolk–shell structured silicon-carbon composite anode preparation via one-step gas-phase deposition and etching technique. *Adv. Funct. Mater.* **2025**, *35*, 2406579.

[18] Jiang, X. Y.; Tang, C. Y.; Zhou, X. C.; Hou, J. W.; Jiang, S.; Meng, L. C.; Zhang, Y. Recent progress in Si/$Ti_3C_2T_x$ MXene anode materials for lithium-ion batteries. *iScience* **2024**, *27*, 111217.

[19] Zeng, S. B.; Lin, Z.; Peng, J.; He, Z. X.; Liang, X. H.; Li, Y. Y.; Lv, Y.; Xiong, L. B. Synergistic structural integrity and remarkable structural stability of NC@Si anodes for lithium-ion batteries. *Mater. Res. Bull.* **2025**, *182*, 113162.

[20] Li, H.; Chen, Q. S.; Feng, L. L.; Zou, Y. L.; Gong, X. Z.; Wang, Z.; Liu, J. H. Vapor-phase conversion of waste silicon powders to silicon nanowires for ultrahigh and ultra-stable energy storage performance. *J. Energy Chem.* **2025**, *102*, 27–36.

[21] Li, J. W.; Wang, T. D.; Wang, Y. J.; Xu, Z. H.; Mateen, A.; Yan, W.; Li, H. J.; Mujear, A.; Chen, J.; Deng, S. Y. et al. Solid–liquid–solid growth of doped silicon nanowires for high-performance lithium-ion battery anode. *Nano Energy* **2025**, *133*, 110455.

[22] Sánchez-Ahijón, E.; Pendashteh, A.; Vilatela, J. J. Paper-like 100% Si nanowires electrodes integrated with argyrodite Li_6PS_5Cl solid electrolyte. *Batter. Supercaps* **2024**, *7*, e202400292.

[23] Cao, Z. J.; Du, Z. G.; Jia, K.; Jin, L.; Li, N.; Zhang, M.; Gao, R.; Abdelkader, A.; Kumar, R. V.; Ding, S. J. et al. Bubbling chemical vapors in molten metal toward XIV-group nanosheets. *Nano Lett.* **2024**, *24*, 14559–14566.

[24] Ren, H. L.; Su, Y.; Zhao, S.; Li, C. W.; Wang, X. M.; Li, B. H. N and B co-doping to enhance Li adsorption and diffusion properties on silicene/graphene heterostructures: Insights from density functional theory. *Mater. Sci. Semicond. Process.* **2025**, *186*, 109041.

[25] Liu, J. J.; Yang, Y.; Lyu, P.; Nachtigall, P.; Xu, Y. X. Few-layer silicene nanosheets with superior lithium-storage properties. *Adv. Mater.* **2018**, *30*, 1800838.

[26] Zhou, J.; Zhao, H. Y.; Lin, N.; Li, T. Q.; Li, Y.; Jiang, S.; Tian, J.; Qian, Y. T. Silicothermic reduction reaction for fabricating interconnected Si-Ge nanocrystals with fast and stable Li-storage. *J. Mater. Chem. A* **2020**, *8*, 6597–6606.

[27] Zheng, G. R.; Xiang, Y. X.; Xu, L. F.; Luo, H.; Wang, B. L.; Liu, Y.; Han, X.; Zhao, W. M.; Chen, S. J.; Chen, H. L. et al. Controlling surface oxides in Si/C nanocomposite anodes for high-performance Li-ion batteries. *Adv. Energy Mater.* **2018**, *8*, 1801718.

[28] Tian, Y. F.; Li, G.; Xu, D. X.; Lu, Z. Y.; Yan, M. Y.; Wan, J.; Li, J. Y.; Xu, Q.; Xin, S.; Wen, R. et al. Micrometer-sized $SiMg_yO_x$ with stable internal structure evolution for high-performance Li-ion battery anodes. *Adv. Mater.* **2022**, *34*, 2200672.

[29] Ji, W. L.; Li, M. H.; Nong, Y. T.; Luo, J.; Liang, X. L.; Wang, X. W.; Ming, L.; Ou, X.; Zhang, J. F.; Zhang, B. et al. Low-temperature de-alloying and unique self-filling interface optimization mechanism of layered silicon for enhanced lithium storage. *Chem. Commun.* **2024**, *60*, 10500–10503.

[30] Takagaki, R.; Yamamoto, C.; Yamanaka, J.; Arimoto, K.; Kurosawa, M.; Hara, K. O. Synthesis and characterization of $CaSi_2$ films for hydrogenated 2D Si nanosheets. *J. Vac. Sci. Technol. A* **2024**, *42*, 053404.

[31] Gu, J. N.; Zhu, Q.; Shi, Y. Z.; Chen, H.; Zhang, D.; Du, Z. G.; Yang,

S. B. Single zinc atoms immobilized on MXene ($Ti_3C_2Cl_x$) layers toward dendrite-free lithium metal anodes. *ACS Nano* **2020**, *14*, 891–898.

[32] Teixeira, H.; Dias, C.; Silva, A. V.; Ventura, J. Advances on MXene-based memristors for neuromorphic computing: A review on synthesis, mechanisms, and future directions. *ACS Nano* **2024**, *18*, 21685–21713.

[33] Liu, Y. R.; Wu, Y.; Wang, X. W. Thermal transports in the MXenes family: Opportunities and challenges. *Nano Res.* **2024**, *17*, 7700–7716.

[34] Zhou, S. Y.; Li, X.; Zhang, Y. L.; Halim, J.; Xu, C.; Rosen, J.; Strømme, M. Drawing highly ordered MXene fibers from dynamically aggregated hydrogels. *Nano Res.* **2024**, *17*, 9815–9821.

[35] Xiang, K.; Wang, Y. J.; Zhuang, Z. C.; Zou, J.; Li, N.; Wang, D. S.; Zhai, T. Y.; Jiang, J. Z. Self-healing of active site in $Co(OH)_2$/MXene electrocatalysts for hydrazine oxidation. *J. Mater. Sci. Technol.* **2024**, *203*, 108–117.

[36] Guan, S. Y.; Yuan, Z. L.; Zhuang, Z. C.; Zhang, H. H.; Wen, H.; Fan, Y. P.; Li, B. J.; Wang, D. S.; Liu, B. Z. Why do single-atom alloys catalysts outperform both single-atom catalysts and nanocatalysts on MXene. *Angew. Chem., Int. Ed.* **2024**, *63*, e202316550.

[37] Zhu, G. Y.; Hou, Y. N.; Lu, J. Q.; Zhang, H. C.; Zhuang, Z. H.; Baig, M. M.; Khan, M. Z.; Akram, M. A.; Dong, S. Y.; Liu, P. MXene decorated 3D-printed carbon black-based electrodes for solid-state micro-supercapacitors. *J. Mater. Chem. A* **2023**, *11*, 25422–25428.

[38] Li, X.; Guan, Q. H.; Zhuang, Z. C.; Zhang, Y. Z.; Lin, Y. H.; Wang, J.; Shen, C. Y.; Lin, H. Z.; Wang, Y. L.; Zhan, L. et al. Ordered mesoporous carbon grafted MXene catalytic heterostructure as Li-ion kinetic pump toward high-efficient sulfur/sulfide conversions for Li–S battery. *ACS Nano* **2023**, *17*, 1653–1662.

[39] Lang, Z. Q.; Zhuang, Z. C.; Li, S. K.; Xia, L. X.; Zhao, Y.; Zhao, Y. L.; Han, C. H.; Zhou, L. MXene surface terminations enable strong metal-support interactions for efficient methanol oxidation on palladium. *ACS Appl. Mater. Interfaces* **2020**, *12*, 2400–2406.

[40] Loaiza, L. C.; Dupré, N.; Davoisne, C.; Madec, L.; Monconduit, L.; Seznec, V. Complex lithiation mechanism of siloxene and germanane: Two promising battery electrode materials. *J. Electrochem. Soc.* **2021**, *168*, 010510.

[41] Lee, C.; Yan, H. G.; Brus, L. E.; Heinz, T. F.; Hone, J.; Ryu, S. Anomalous lattice vibrations of single- and few-layer MoS_2. *ACS Nano* **2010**, *4*, 2695–2700.

[42] Ismail, M. M.; Vigneshwaran, J.; Arunbalaji, S.; Mani, D.; Arivanandhan, M.; Jose, S. P.; Jayavel, R. Antimonene nanosheets with enhanced electrochemical performance for energy storage applications. *Dalton Trans.* **2020**, *49*, 13717–13725.

[43] Xu, Z. L.; Gang, Y.; Garakani, M. A.; Abouali, S.; Huang, J. Q.; Kim, J. K. Carbon-coated mesoporous silicon microsphere anodes with greatly reduced volume expansion. *J. Mater. Chem. A* **2016**, *4*, 6098–6106.

[44] Gohier, A.; Laïk, B.; Kim, K. H.; Maurice, J. L.; Pereira-Ramos, J. P.; Cojocaru, C. S.; Van, P. T. High-rate capability silicon decorated vertically aligned carbon nanotubes for Li-ion batteries. *Adv. Mater.* **2012**, *24*, 2592–2597.

[45] Agyeman, D. A.; Song, K.; Lee, G. H.; Park, M.; Kang, Y. M. Carbon-coated Si nanoparticles anchored between reduced graphene oxides as an extremely reversible anode material for high energy-density Li-ion battery. *Adv. Energy Mater.* **2016**, *6*, 1600904.

[46] Li, Z. W.; Han, M. S.; Yu, J. Sub-nanometer structured silicon-carbon composite nanolayers armoring on graphite for fast-charging and high-energy-density lithium-ion batteries. *Rare Metals* **2023**, *42*, 3692–3704.

[47] Zhang, W. Y.; Shi, H. F.; Wang, C. D.; Wang, J. S.; Wang, Z.; Jiang, H.; Xiong, Z. H.; Wang, Z. K.; Bai, Z. M.; Yan, X. Q. Synthesizing copper-doped silicon/carbon composite anode as cost-effective active materials for Li-ion batteries. *J. Phys. Chem. Solids* **2023**, *179*, 111387.

[48] Liang, B.; Liu, Y. P.; Xu, Y. H. Silicon-based materials as high capacity anodes for next generation lithium ion batteries. *J. Power Sources* **2014**, *267*, 469–490.

[49] Chen, Y. F.; Du, N.; Zhang, H.; Yang, D. R. Facile synthesis of uniform MWCNT@Si nanocomposites as high-performance anode materials for lithium-ion batteries. *J. Alloy. Compd.* **2015**, *622*, 966–972.

[50] Zhou, M.; Cai, T. W.; Pu, F.; Chen, H.; Wang, Z.; Zhang, H. Y.; Guan, S. Y. Graphene/Carbon-coated Si nanoparticle hybrids as high-performance anode materials for Li-ion batteries. *ACS Appl. Mater. Interfaces* **2013**, *5*, 3449–3455.

[51] Ge, M. Y.; Lu, Y. H.; Ercius, P.; Rong, J. P.; Fang, X.; Mecklenburg, M.; Zhou, C. W. Large-scale fabrication, 3D tomography, and lithium-ion battery application of porous silicon. *Nano Lett.* **2014**, *14*, 261–268.

[52] Wang, Z. Y.; Jing, L. Y.; Zheng, X.; Xu, Z. G.; Yuan, Y. P.; Liu, X. H.; Fu, A. P.; Guo, Y. G.; Li, H. L. Microspheres of Si@Carbon-CNTs composites with a stable 3D interpenetrating structure applied in high-performance lithium-ion battery. *J. Colloid Interface Sci.* **2023**, *629*, 511–521.